


High-Speed Large-Field Multifocal Illumination Fluorescence Microscopy

Journal Article**Author(s):**

Chen, Zhenyue; Mc Larney, Benedict; Rebling, Johannes; Dean-Ben, Xose Luis; Zhou, Quanyu; Gottschalk, Sven; Razansky, Daniel 

Publication date:

2020-02

Permanent link:

<https://doi.org/https://doi.org/10.3929/ethz-b-000387371>

Rights / license:

[Creative Commons Attribution-NonCommercial 4.0 International](#)

Originally published in:

Laser & Photonics Reviews 14(2), <https://doi.org/10.1002/lpor.201900070>

High-Speed Large-Field Multifocal Illumination Fluorescence Microscopy

Zhenyue Chen, Benedict Mc Larney, Johannes Rebling, Xosé Luis Deán-Ben, Quanyu Zhou, Sven Gottschalk, and Daniel Razansky*

Scanning optical microscopy techniques are commonly restricted to a sub-millimeter field-of-view (FOV) or otherwise employ slow mechanical translation, limiting their applicability for imaging fast biological dynamics occurring over large areas. A rapid scanning large-field multifocal illumination (LMI) fluorescence microscopy technique is devised based on a beam-splitting grating and an acousto-optic deflector synchronized with a high-speed camera to attain real-time fluorescence microscopy over a centimeter-scale FOV. Owing to its large depth of focus, the approach allows noninvasive visualization of perfusion across the entire mouse cerebral cortex, not achievable with conventional wide-field fluorescence microscopy methods. The new concept can readily be incorporated into conventional wide-field microscopes to mitigate image blur due to tissue scattering and attain optimal trade-off between spatial resolution and FOV. It further establishes a bridge between conventional wide-field macroscopy and laser scanning confocal microscopy, thus it is anticipated to find broad applicability in functional neuroimaging, in vivo cell tracking, and other applications looking at large-scale fluorescent-based biodynamics.

1. Introduction

Owing to its high molecular specificity, excellent contrast, and spatial resolution, fluorescence microscopy has become a workhorse of the modern biological discovery.^[1–3] With the advent of high-speed cameras, wide-field fluorescence microscopes are now capable of achieving kilohertz (kHz) imaging speeds when tracking fast biological dynamics. However, the effective resolving capacity of traditional wide-field microscopes is severely impaired when imaging through scattering objects.^[4] High-resolution transcranial optical cerebrovascular imaging was reported based on laser speckle and dynamic fluorescence imaging.^[5] Yet, the reconstruction involved analysis of long image sequences, which compromised the effective temporal resolution and hindered visualization of fast perfusion. Moreover, high photo-bleaching rates associated with

continuous light exposure of the entire imaged sample may hamper observations of longitudinal dynamics.^[6]

Recently, the use of short-wave infrared (SWIR) or second near-infrared window (NIR-II) has been proposed for noninvasive, deep-tissue visualization. Compared to the first near-infrared window (NIR-I), longer wavelengths in NIR-II greatly mitigate photon scattering and can facilitate greater penetration depth with higher image contrast due to reduced autofluorescence.^[7] However, the application of SWIR to biological imaging is restricted by limited availability and low quantum efficiency of fluorescent agents in this spectral range.^[8]


The effects of scattering and photobleaching in fluorescent microscopy can be further minimized by employing scanning-based approaches. To this end, a large number of scanning microscopy techniques have been developed and are widely used in biomedical research. In single point scanning methods, such as laser scanning confocal microscopy (LSCM)^[9,10] or two-photon microscopy (2PM),^[11,12] the fluorescent signal is selectively generated or detected from a diffraction-limited focal spot. Stimulated emission depletion (STED) microscopy has further enabled breaking through the optical diffraction barrier by attaining super-resolution imaging.^[13,14] Single point scanning methods are, however, not suitable for imaging fast processes and efforts are underway to boost imaging speeds by employing

Dr. Z. Chen, J. Rebling, Dr. X. L. Deán-Ben, Q. Zhou, Prof. D. Razansky
Faculty of Medicine and Institute of Pharmacology and Toxicology
University of Zurich
8057 Zurich, Switzerland
E-mail: daniel.razansky@uzh.ch

Dr. Z. Chen, J. Rebling, Dr. X. L. Deán-Ben, Q. Zhou, Prof. D. Razansky
Institute for Biomedical Engineering and Department of Information
Technology and Electrical Engineering
ETH Zurich 8093 Zurich, Switzerland

B. Mc Larney, Dr. S. Gottschalk, Prof. D. Razansky
Institute for Biological and Medical Imaging
Helmholtz Center Munich
Neuherberg 85764, Oberschleißheim, Germany

B. Mc Larney, Prof. D. Razansky
Faculty of Medicine
Technical University of Munich
81675 Munich, Germany

 The ORCID identification number(s) for the author(s) of this article can be found under <https://doi.org/10.1002/lpor.201900070>

© 2019 The Authors. Published by WILEY-VCH Verlag GmbH & Co. KGaA, Weinheim. This is an open access article under the terms of the Creative Commons Attribution-NonCommercial License, which permits use, distribution and reproduction in any medium, provided the original work is properly cited and is not used for commercial purposes.

DOI: 10.1002/lpor.201900070

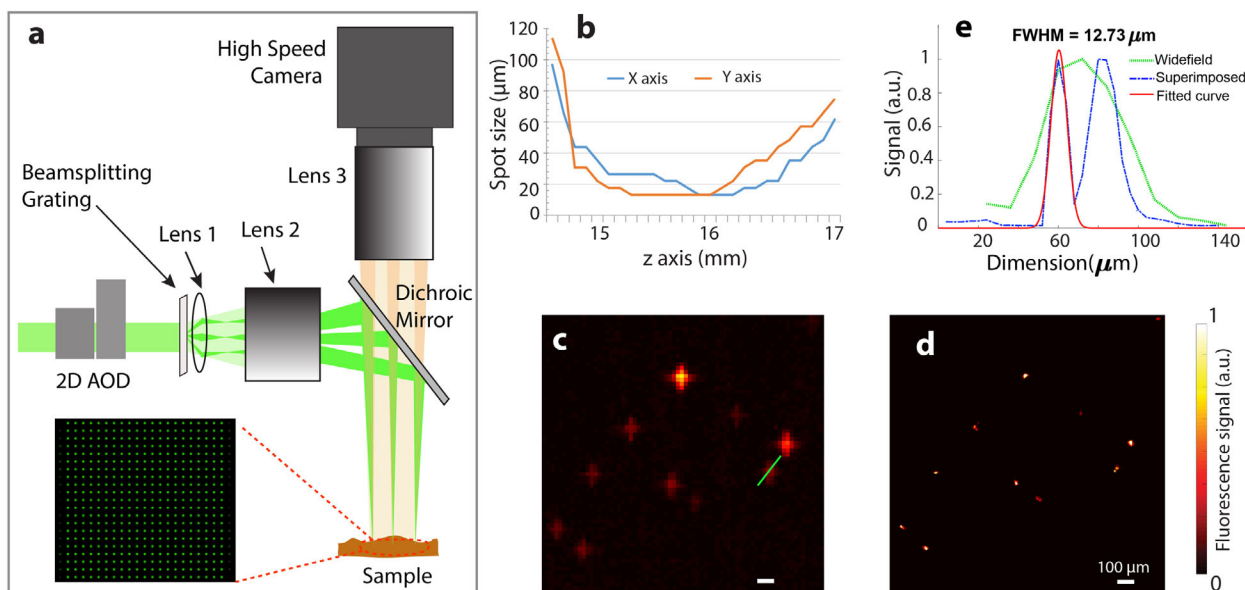


Figure 1. System setup and characterization. a) Schematic diagram of the large-field multifocal illumination (LMI) microscopy system consisting of an acousto-optic deflector (AOD), beam-splitting grating, focusing assembly, and a high-speed fluorescence camera. The inset in the bottom left corner shows the picture of illumination grid when a 21×21 beam-splitting grating is employed. In this case, an inter-beam angle of 0.57° is achieved while raster scanning the multifocal illumination pattern both in horizontal and vertical planes renders a high-resolution image over a large FOV. b) Plot of the spot size estimated along the axial (z) direction, indicating > 1 mm depth of focus (DOF). c) Conventional wide-field fluorescence image of the agar phantom containing $10\text{-}\mu\text{m}$ -diameter fluorescence beads. d) The corresponding LMI image reconstructed from the same target. e) Line profiles along the green line indicated in (c). The red Gaussian-fitted curve shows that the LMI system has an effective spatial resolution of $12.73\ \mu\text{m}$.

fast-scanning components, such as mechanical stages, micro-electro-mechanical systems (MEMS), galvanometer mirrors, and acousto-optic deflectors.^[15–18]

The imaged field-of-view (FOV) that can be efficiently covered per unit time is further determined by the size of the focal light spot. Thus, volumetric imaging rates can be ramped up by giving up on the spatial resolution.^[19] For example, the focal spot in 2PM can be smeared using sculpted light.^[20] Recent efforts in optical microscopy have additionally been devoted to other methodologies that attain high-frame-rate volumetric imaging, for example, light sheet^[21,22] or light field^[23,24] microscopy. Hybrid opto-acoustic tomography and microscopy systems have recently demonstrated powerful large-scale volumetric imaging performance,^[25,26] outperforming the speed^[27] and sensitivity of fluorescence readings at deeper locations in living scattering tissues.^[28]

Parallel acquisition methods represent an alternative approach for accelerating imaging by simultaneously illuminating larger areas or generating multiple foci. For instance, spinning disk confocal microscopy (SDCM) utilizes multiple pinholes or slits to project a series of 1000 or more parallel excitation foci onto the sample in a multiplexed pattern.^[29,30] Parallelized multi-beam STED has enabled video-rate nanoscopy recordings via 2000-fold acceleration of the imaging speed.^[31] Simultaneous scanning of separate regions has been suggested for visualizing large areas with 2PM.^[32,33] Structured illumination microscopy (SIM) arguably offers the highest degree of parallelization as only a relatively small number of wide-field images are required for rendering a super-resolution image. State-of-the-art SIM can achieve imaging rates of 79 frames per second for a region of interest (ROI) of $16.5 \times 16.5\ \mu\text{m}^2$.^[34] Recent progress on multifocal

SIM enabled 3D interrogation of live organisms at frame rates of ~ 1 Hz, covering a FOV in the $50\text{--}100\ \mu\text{m}$ range.^[35–37] However, the existing scanning-based parallel acquisition methods are only applicable for imaging very small areas with high resolution, so that wide-field approaches remain the method of choice for large-scale imaging. Here, linear motor stages are commonly employed to scan larger areas where FOVs on the order of $50\ \text{mm}^2$ were showcased for ex vivo samples at the expense of lengthy data acquisition on the order of tens of minutes.^[38,39]

Here, we propose a large-field multifocal illumination (LMI) scanning microscopy method based on an acousto-optic deflector (AOD) and a beam-splitting grating. The laser beam is raster scanned by the AOD running at kHz scanning rate with the beam split into hundreds of mini-beams, which are subsequently focused by a condensing lens and a macroscopic objective to generate multifocal illumination. The excited fluorescence signal is synchronously collected by a high-speed camera with the signals then combined into a high-resolution image.

2. Experimental Section

2.1. Experimental Setup

Figure 1a depicts the schematic diagram of the LMI imaging system. A high pulse repetition frequency (PRF) Q-switched, diode end-pumped Nd:YAG laser (model: IS8II-E, EdgeWave, Germany) operating at $532\ \text{nm}$ wavelength was used for excitation. The PRF of the laser was adjustable within the $200\text{--}10\ \text{kHz}$ range. The laser beam was first scanned by the AOD (AA Opto-Electronic, France) and then guided into a customized

beam-splitting grating (Holoeye GmbH, Germany) to generate multiple mini-beams. The custom-made gratings were manufactured with different diffraction orders, such as -7 to $+7$ orders and -10 to $+10$ orders, and had a diffraction efficiency of $\approx 74\%$ and intensity uniformity within $\pm 10\%$ for all the diffraction orders. The angle between adjacent diffraction orders was 0.57° , smaller than the maximum scanning angle of 2.292° of the AOD. The mini-beams were relayed by Lens 1 to the input pupil of Lens 2 and then focused onto the sample to generate multiple foci. After passing through the dichroic mirror, the emitted fluorescence signal was collected by Lens 3 and then focused onto the sensor plane of a high-speed camera (pco.dimax S1, PCO AG, Germany). The PCO camera had frame rate up to 4467 fps at full pixel resolution of 1008×1008 pixels. During data acquisition, a NI-PCIe 6535b DIO (National Instrument, USA) was employed to synchronize the data transfer of the AOD and trigger signals for the laser pulse and camera acquisition. Since the AOD had 15-bit scanning accuracy within the full scan angle, raster scanning the multifocal illumination pattern both in horizontal and vertical planes resulted in a high-resolution image.

2.2. Image Reconstruction

The first step in the image post-processing chain included identification of the local maxima in each scanning frame. Since the illumination pattern was well defined and the pixel distances between adjacent spots were approximately known, this step facilitated extraction of usable data while discarding random noise. A weighted centroid was calculated for each spot in order to perform upsampling. The upsampling ratio was calculated according to the pixel distance between adjacent spots and the number of scanning steps. For instance, an upsampling ratio of 5 was applied for 20 inter pixel distance and 100 scanning steps. For signal extraction in each scanning frame, only pixels within the circles defined by the centroids and a pre-defined radius would be selected. In this way, virtual pin-holes were applied to each spot while the surrounding pixels introduced by the out of focus light would be zeroed out. The extracted signals were subsequently copied and superimposed onto the upsampled image at locations of their corresponding centroids. Correction for the nonuniform beam intensity profile was performed across each frame before combining the image values of local maxima to form the complete high-resolution image. The intensity distribution of the diffracted beam was measured using a beam profiler (SP620u, Ophir Optonics, USA). Note that laser pulse energy fluctuations and other aberrations caused by optical components might necessitate additional corrections to obtain finetuned image quality and more uniform responsivity; however, no such corrections were applied here.

2.3. Phantom Experiment

To evaluate the LMI system performance, 10 μm - and 75 μm -diameter orange polystyrene fluorescent beads (540/560) were imaged (FluoSpheres, Thermo Fisher Scientific and UVPMS-BO-1.00 63–75 μm , Cosphere LLC, USA). For this, agar phantoms were molded into a Petri dish by adding 0.65 g agar powder

to 50 mL distilled water. The beads were added and stirred to obtain a homogenous mixture. A 21×21 beam-splitting grating and a 35 mm plano-convex lens and a Nikkor 35 mm f/2D lens (Lens 1) were employed to generate the multifocal illumination pattern. A 2-inch dichroic mirror (DMLP567L, Thorlabs, USA) separated the emission light from the excitation. A Nikkor 105 mm f/2.8D AF Micro Nikkor lens (Lens 2) collected the emitted signal. The PCO camera was operated at 4 kHz in external trigger mode synchronized with the laser pulses and the AOD beam scanning. To characterize the spatial resolution of the system, a phantom consisting of 10 μm -diameter beads was raster scanned along two axes over 200×200 scanning positions with 3.3 μm scanning step size, the latter corresponding to the 660 μm distance between two adjacent spots divided by the number of scanning positions. Another phantom consisting of 75 μm -diameter beads phantom was scanned over 35×35 positions (28 μm step size, 1 mm distance between adjacent spots), whereas rendering of a high-resolution image over $20 \times 20 \text{ mm}^2$ FOV lasted 0.306 s.

2.4. In Vivo Animal Experiment

The proposed method was subsequently validated in vivo by imaging the brain of athymic nude-Fox1nu mice (Harlan Laboratories LTD, Switzerland) following a tail-vein injection of 10 μL of 1 mg mL^{-1} ($\sim 138 \mu\text{M}$) Alexa Fluor 532 carboxylic acid (Thermo Fisher Scientific, USA) solution in water. The mice were anesthetized with isoflurane (2.5% v/v for induction and 1.5–2.0% v/v during experiments) in 100% O_2 at a flow rate of $\sim 0.8 \text{ L min}^{-1}$. The first experiment was performed with a 2-month-old mouse with intact skull while the scalp was removed to reduce light scattering. In this case, to minimize bleeding, hemostatic sponges (Gelfoam, Pfizer Pharmaceutical) were used together with a topical application of adrenaline. After the experiment, the animal was euthanized while still being under anesthesia. The second experiment was performed on a 2-month-old mouse with both its scalp and skull intact, that is, entirely noninvasively. Animal handling and experimentation were conducted in full accordance with the directives on animal experimentation of the Helmholtz Center Munich and with approval from the Government District of Upper Bavaria. The same imaging setup was used for both phantom and in vivo experiments. However, in the latter case, the distance between adjacent spots was set at 600 μm while either 25×25 (24 μm step size) or 15×15 (40 μm step size) scanning patterns were employed in order to increase the imaging speed. The laser output on the sample was measured at $\sim 125 \mu\text{J}$ per pulse (i.e., $\sim 0.28 \mu\text{J}$ per pulse for each mini-beam) to compensate for a relatively weak fluorescent signal and strong scattering by different tissue layers. After concluding the LMI data acquisition, each mouse received a second dye injection while fluorescence images were recorded with conventional wide-field fluorescence method for comparison.

3. Results and Discussion

Figure 1a depicts the schematic diagram of the imaging system which is based on a beam-splitting grating and an acousto-optic deflector synchronized with a high-speed camera. The multi-beam pattern generated by the beam-splitting grating is focused

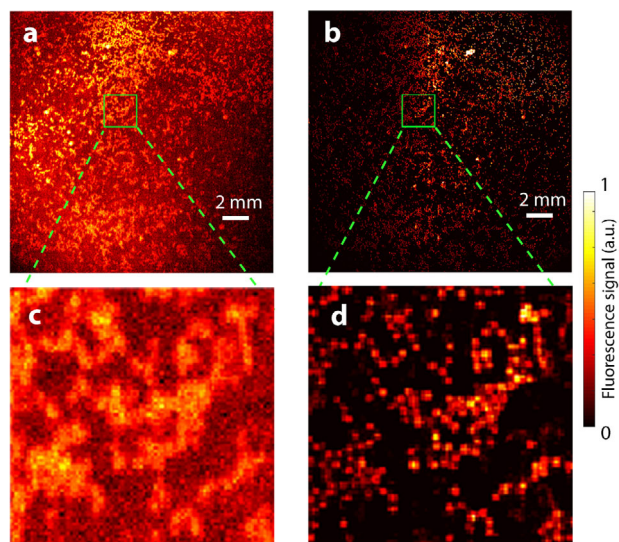


Figure 2. Experimental LMI imaging results from agar phantom embedded with 75- μm -diameter fluorescent orange polyethylene beads. a) Conventional wide-field image of the phantom. b) LMI image combining 35 \times 35 raster scanned frames. The zoom-ins in c) and d) clearly demonstrate superiority of the LMI method in terms of image contrast and spatial resolution.

by a condensing lens (Lens 1) and a macroscopic objective (Lens 2) to generate a multifocal structured illumination profile on the imaged sample that is rapidly scanned at kHz rates. The grid pattern of the diffracted beam measured with a beam profiler exhibited good uniformity with the individual spots having $\sim 20\ \mu\text{m}$ diameter within $\sim 1\ \text{mm}$ DOF, as shown in Figure 1b. Figure 1c shows a small portion of the wide-field image of the 10 μm diameter fluorescent beads and Figure 1d shows the corresponding fully reconstructed image after 200 \times 200 raster scanning. Figure 1e shows the comparison of the line profile in both images at a location indicated by the green line in Figure 1c. Due to the given magnification power of the 105 mm Nikon lens and the 11 μm pixel size of the CMOS sensor, the effective spatial resolution for wide-field imaging is determined by the resulting 23 μm patch per pixel. However, in the reconstructed upsampled image in Figure 1d, the patch size is reduced to 3.8 μm . Thus, two beads within a 23 μm distance can be distinguished and the Gaussian fitted curve in Figure 1e shows that the system has an effective spatial resolution of 12.73 μm .

Figure 2 displays images acquired from the phantom containing 75- μm -diameter fluorescent beads. Due to light scattering by the bulk agar sample, the wide-field image in Figure 2a appears blurred while the LMI image (Figure 2b) obtained by stitching 35 \times 35 scanning frames exhibits superior spatial resolution and contrast, as can be further verified by inspecting the zoom-ins in Figures 2c,d. The entire LMI image rendering process can be viewed in Video S1, Supporting Information.

Figure 3 displays the time-lapse imaging results from the tail-vein injection of Alexa Fluor 532 fluorescent dye. Note that both in vivo experiments were performed transcranially while in the first experiment, the scalp was removed to reduce light scattering. As expected, the conventional wide-field images (Figure 3a) are blurred due to the strong light scattering in the mouse brain,

rendering its cerebral vascular anatomy hardly distinguishable. On the contrary, the LMI images acquired by combining 15 \times 15 = 225 scanning steps (Figure 3b) exhibit excellent contrast and spatial resolution through the intact skull while also accurately resolving the perfusion process in the deeply embedded cerebral microvasculature. The same average laser output power was used in both cases. We then reconstructed the entire vascular tree by combining maximum pixel intensities across the temporal LMI image sequence (Figure 3c), encoding it as intensity and saturation.^[40] Time to peak analysis (Figure 3d) further reveals the contrasting perfusion behavior. For instance, the sinusoidal vascular networks, presumably belonging to the skull, exhibit much longer perfusion constants. The poor visibility of parts of the sagittal sinus can be further ascribed to the dense calvarian vasculature as well as light aberrations in the irregular skull suture structures. Note that the significant spatial blurring of the conventional wide-field fluorescence also introduces smearing into the perfusion signal profiles (Figure 3e) while signal profiles from LMI images (Figure 3f) can better represent the perfusion dynamics. The dynamic LMI visualization of the entire perfusion process is further shown in Video S2, Supporting Information.

Figure 4 displays the results of the noninvasive (scalp intact) imaging experiment. Despite the younger mouse age, strong scattering by the skin results in a more significant blurring so that cerebral vasculature becomes unrecognizable in the regular wide-field images (Figure 4a). On the other hand, the LMI images reconstructed by combining 25 \times 25 = 625 scanning steps maintain superior image contrast and spatial resolution through the intact scalp and skull (Figure 4b). When comparing the results to experiments shown in Figure 3, the scalp presence does greatly affect the LMI performance, both in terms of its spatial resolving capacity (Figures 4b,c) as well as temporal profiles (Figures 4e,f). Nevertheless, similar perfusion dynamics are manifested in both cases with the anterior and middle cerebral arteries lighting up at an earlier time point as compared to the superior sagittal sinus. Note that additional small vessels, not present in Figure 3, appear at later time points (Figure 4d), which can be attributed to the skin vasculature. Noninvasive dynamic visualization of the fluorescent dye perfusion is further available in Video S3, Supporting Information.

High temporal resolution is crucial when it comes to imaging rapid biological dynamics in, for example, freely behaving organisms, heart motion, fast perfusion, neural activity, to name a few. Imaging rates of conventional scanning optical microscopy methods are determined by the scanning speed of the laser beam. For instance, in MEMS- or piezo-based scanning systems, the speed limitations chiefly arise from inertia associated with the mass of rotating mirrors and other moving parts. Modern AODs can achieve megahertz scanning speeds, thus allowing random access with high accuracy. Yet, their major drawback is the small deflection angles (typically $<0.05\ \text{rad}$) and limited resolvable number of spots (typically <500).^[41] Here, we capitalized instead on the large diffraction angle and the multi-beams strategy introduced by the beam-splitting grating. When employing 21 \times 21 beam-splitting grating, the maximum deflection angle has been effectively expanded by 5.7 $^\circ$ while the number of resolvable spots has correspondingly grown by the factor of 21 \times 21. Note that both the deflection angle and the resolvable spots can be

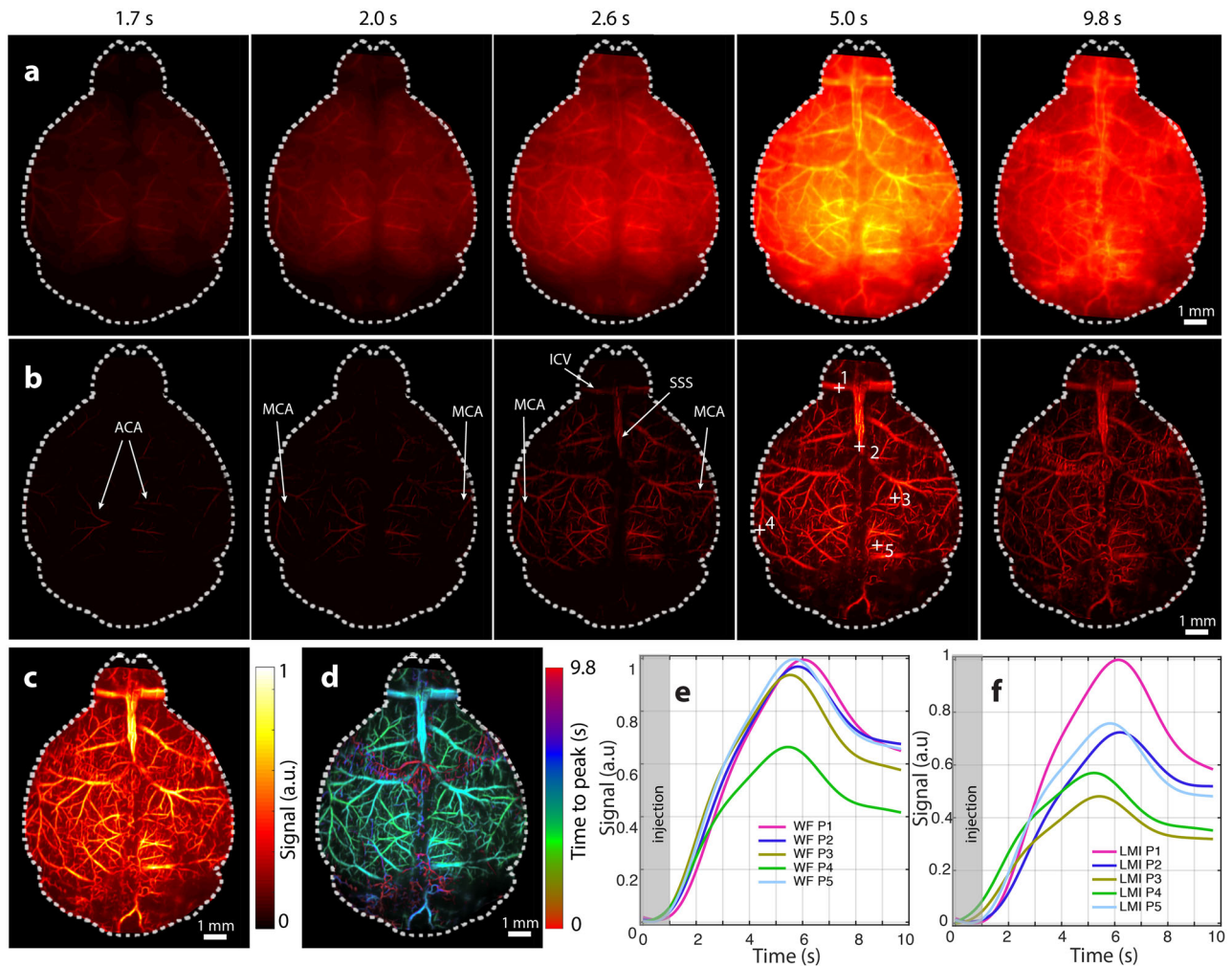


Figure 3. Real-time transcranial visualization of Alexa Fluor 532 fluorescent dye perfusion across the entire mouse brain cortex. a) Time-lapse sequence of conventional wide-field fluorescence images. b) The corresponding LMI image sequence acquired with a 15×15 scanning pattern, that is, ten frames per second full image rate at 2.25 kHz laser pulse repetition rate. Some major vessels are labeled: ACA, anterior cerebral artery; MCA, middle cerebral artery; SSS, superior sagittal sinus; ICV, inferior cerebral vein. c) Temporal maximum intensity projection of the LMI image sequence, encoded as intensity and saturation. d) The corresponding time to peak map. e, f) Temporal perfusion profiles in the corresponding areas P1–P5 of the wide-field fluorescence images and LMI images, as indicated in panel (b). WF, wide-field image; LMI, large-field multifocal illumination image. Scale bar 1 mm.

further increased by employing higher-order diffraction gratings yet at the expense of more complex manufacturing processes.

The general concept of employing multiple foci to accelerate microscopic data acquisition has previously been explored.^[42,43] However, the strategy of generating the multiple foci with a microlens array has greatly compromised the imaging speed since the array is mechanically scanned to cover the entire FOV. Besides, millimeter or sub-millimeter work distance had to be imposed in order to obtain a relatively large NA of the excitation beam, making the concept impractical for in vivo biological studies. Other strategies, such as employing a digital mirror device (DMD) or a grid pattern to generate the multifocal illumination, are less efficient since most of the light is rejected whereas the limited size of DMD or grid pattern further restricts the achievable FOV. In contrast, our solution provides an efficient and flexible way of attaining an optimal trade-off between spatial resolution and FOV with large scalability, from micro- to macroscales.

The achievable image acquisition rate of the proposed LMI method is mainly determined by the camera speed and the laser PRF. Thus, the effective frame rate can be further improved by: 1) reducing the FOV so that less scanning steps are required to form one combined LMI image. Since commercial Nikon lenses are employed in the system, the illumination and imaging work distance can be readily adjusted to attain FOVs between 7 mm up to several centimeters across; 2) employing a higher-order beam-splitting grating (e.g., 101×101) would generate 10,201 individual beams, thus boosting the data acquisition rates by a factor of 23 as compared to the 21×21 grating only having 441 individual beams. Note that the output power of the laser has to be increased accordingly in this case; (3) multiple scans of the illumination pattern can potentially be integrated to form one camera frame, as long as the adjacent spots are well separated in the integrated camera frame. In our current LMI implementation, the laser has a PRF of up to 10 kHz and its pulse width is

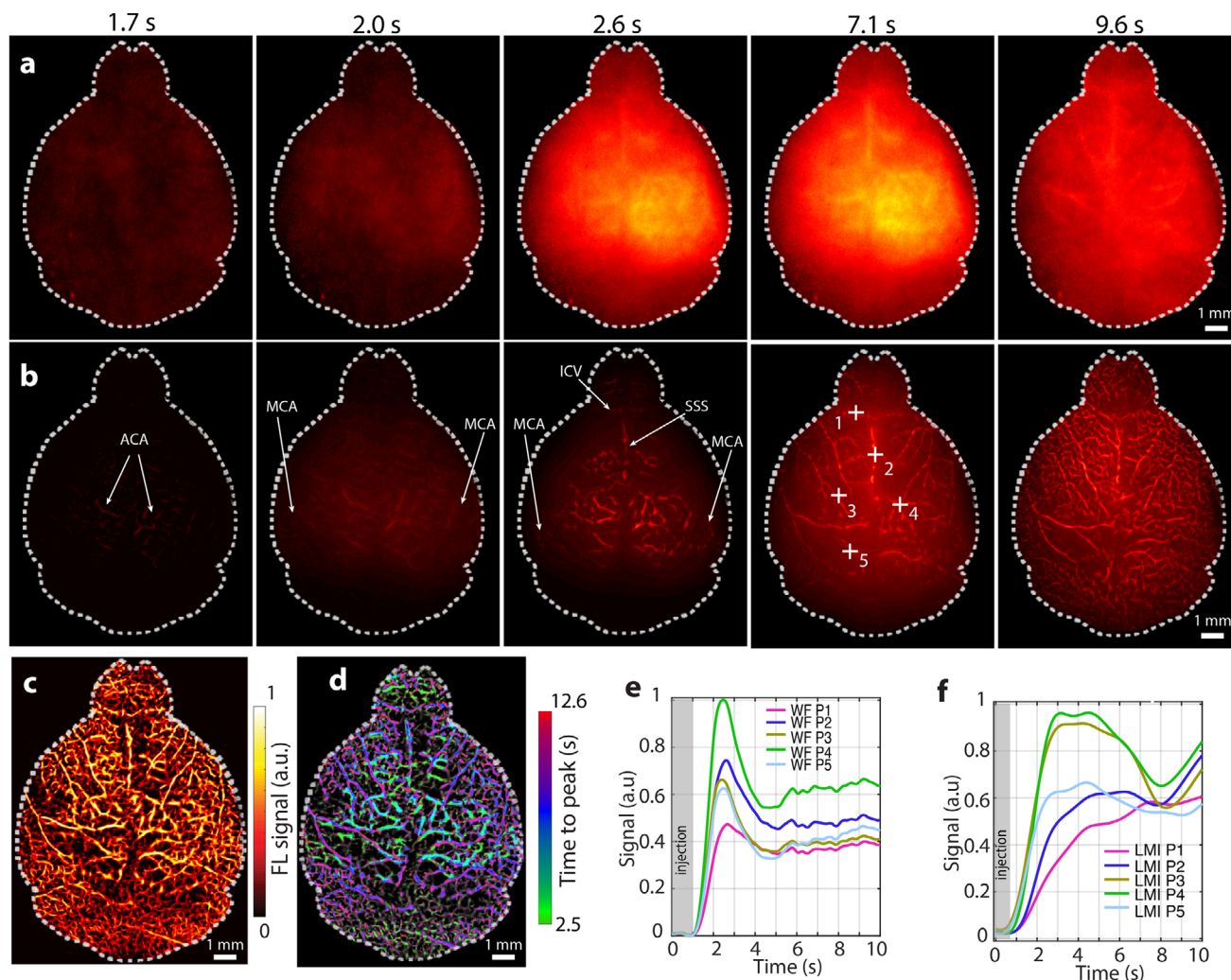


Figure 4. Noninvasive visualization of the fluorescent dye perfusion in the mouse brain. a) Conventional wide-field fluorescence images. b) LMI images acquired with a 25×25 scanning pattern at 1 kHz frame rate. Some major vessels are labeled: ACA, anterior cerebral artery; MCA, middle cerebral artery; SSS, superior sagittal sinus; ICF, inferior cerebral vein. c) Temporal maximum intensity projection of the LMI image sequence, encoded as intensity and saturation. d) The corresponding time to peak map. e, f) Temporal perfusion profiles in the corresponding areas P1–P5 of the wide-field fluorescence images and LMI images whose locations are indicated in panel (b). Scale bar 1 mm.

~ 10 ns whereas the high-speed camera has a 4.4 kHz frame rate at full resolution. By increasing the laser PRF, one may potentially render combined LMI images at frame rates effectively limited by the camera speed. Furthermore, since thousands of foci are employed for simultaneous excitation in each scan, the pixel dwell time is accordingly increased thousands fold as compared to LSCM, resulting in tremendous improvement of the image SNR per given average power levels. Besides, due to the higher quantum efficiency of the high-speed camera as compared with the photomultiplier tubes typically employed for the LSCM (QE < 40%), higher photon detection efficiency can be achieved, which will further reduce photobleaching and phototoxicity.

When comparing to SDCM, the LMI technique similarly employs multiple foci for the excitation. However, LMI is a more versatile method, less complex to implement, and easier to be adopted by wide-field microscopes. The pinhole diameters in SDCM are fixed, resulting in significant crosstalk between the

neighboring pinholes. Therefore, one has to space the pinholes considerably to avoid crosstalk between the individual beams, which inevitably decreases the excitation light throughput.^[30] Besides, the maximum imaging speed of SDCM is restricted to 1/12 of the spinning disk rotation frequency, leading to significantly slower scanning speed in comparison with AODs.^[30] Although sinusoidal SIM techniques require fewer illumination patterns, they are unable to physically reject out-of-focus light, therefore, optical sectioning is solely achieved with computational processing. In LMI, the out-of-focus background is inherently rejected (reduced) by the hardware. Additionally, due to the small NA of the individual pencil-like beams, the depth of focus (DOF) of the illumination light is greatly increased, making the system especially powerful for imaging large samples with curved surfaces, such as the intact mouse brain.

It should be noted that the current LMI implementation is optimized for resolving rapid dynamics over large 2D FOVs. In

order to resolve depth-dependent information via 3D scanning, the numerical aperture of the optical system must be adjusted to large values, which would readily result in a small FOV. In addition, depth scanning implies slower imaging speed, leading to an inevitable tradeoff between axial and lateral resolution, field-of-view, and imaging speed.

4. Conclusions and Outlook

In conclusion, we propose a rapid scanning large-field fluorescence microscopy method based on multifocal illumination and acousto-optic beam steering. The powerful combination between large FOV ($20 \times 20 \text{ mm}^2$), enhanced DOF ($>1 \text{ mm}$), and real-time imaging performance has been achieved. The noninvasive in vivo mouse brain imaging results further demonstrate the superior performance of LMI for imaging highly scattering, large-scale object with a curved surface. By employing higher-order beam-splitting gratings, faster cameras and lasers, our future work is aimed at achieving finer resolution and increasing the effective imaging rates to the hundreds of Hz range, thus facilitating observation of faster bio-dynamics, such as rapid calcium and voltage activity and stimulus evoked brain responses. The proposed method establishes a bridge between conventional wide-field macroscopy and laser scanning confocal microscopy, thus anticipated to find broad applicability in functional neuroimaging, in vivo tracking of cells and other applications looking at large-scale fluorescent-based biodynamics.

Supporting Information

Supporting Information is available from the Wiley Online Library or from the author.

Acknowledgements

The authors would like to thank M. Reiss and U. Klemm for the assistance in animal experimentation. This project has received funding from the European Union's Horizon 2020 research and innovation program under the Marie Skłodowska-Curie Grant Agreement No. 746430 - MSIOAM and the European Research Council Consolidator Grant ERC-2015-CoG-682379.

Conflict of Interest

The authors declare no conflict of interest.

Keywords

diffraction gratings, fast scanning microscopy, fluorescence imaging, multifocal illumination

Received: February 27, 2019

Revised: September 20, 2019

Published online: December 23, 2019

- [1] G. C. H. Mo, *Nat. Methods* **2017**, *14*, 427.
- [2] B. J. Beliveau, *Nat. Commun.* **2015**, *6*, 7147.
- [3] P. Sengupta, *Nat. Methods* **2011**, *8*, 969.
- [4] V. Ntziachristos, *Nat. Methods* **2010**, *7*, 603.
- [5] V. Kalchenko, D. Israeli, Y. Kuznetsov, I. Meglinski, A. Harmelin, *J. Biophotonics* **2015**, *8*, 897.
- [6] C. Boudreau, T. E. Wee, Y. S. Duh, M. P. Couto, K. H. Ardakani, C. M. Brown, *Sci. Rep.* **2016**, *6*, 30892.
- [7] G. Hong, S. Diao, J. Chang, A. L. Antaris, C. Chen, B. Zhang, S. Zhao, D. N. Atochin, P. L. Huang, K. I. Andreasson, C. J. Kuo, H. Dai, *Nat. Photonics* **2014**, *8*, 723.
- [8] A. L. Antaris, H. Chen, K. Cheng, Y. Sun, G. Hong, C. Qu, S. Diao, Z. Deng, X. Hu, B. Zhang, X. Zhang, O. K. Yaghi, Z. R. Alamparambil, X. Hong, Z. Cheng, H. Dai, *Nat. Mater.* **2016**, *15*, 235.
- [9] M. Minsky, *Scanning* **1988**, *10*, 128.
- [10] S. Hell, E. H. K. Stelzer, *J. Opt. Soc. Am. A* **1992**, *9*, 2159.
- [11] I. D. Abella, *Phys. Rev. Lett.* **1962**, *9*, 453.
- [12] W. Kaiser, C. G. B. Garrett, *Phys. Rev. Lett.* **1961**, *7*, 229.
- [13] K. I. Willig, S. O. Rizzoli, V. Westphal, R. Jahn, S. W. Hell, *Nature* **2006**, *440*, 935.
- [14] T. A. Klar, S. Jakobs, M. Dyba, A. Egner, S. W. Hell, *Proc. Natl. Acad. Sci. USA* **2000**, *97*, 8206.
- [15] J. Wu, A. H. L. Tang, A. T. Y. Mok, W. Yan, G. C. F. Chan, K. K. Y. Wong, K. K. Tsia, *Biomed. Opt. Express* **2017**, *8*, 4160.
- [16] Q. Geng, C. Gu, J. Cheng, S. Chen, *Optica* **2017**, *4*, 674.
- [17] N. J. Sofroniew, D. Flickinger, J. King, K. Svoboda, F. Rieke, *eLife* **2016**, *5*, e14472.
- [18] R. Salomé, Y. Kremer, S. Dieudonné, J. F. Léger, O. Krichevsky, C. Wyart, D. Chatenay, L. Bourdieu, *J. Neurosci. Methods* **2006**, *154*, 161.
- [19] A. Cheng, J. T. Gonçalves, P. Golshani, K. Arisaka, C. Portera-Cailliau, *Nat. Methods* **2011**, *8*, 139.
- [20] R. Prevedel, A. J. Verhoef, A. J. Pernia-Andrade, S. Weisenburger, B. S. Huang, T. Nobauer, A. Fernandez, J. E. Delcour, P. Golshani, A. Baltuska, A. Vaziri, *Nat. Methods* **2016**, *13*, 1021.
- [21] M. B. Bouchard, V. Voleti, C. S. Mendes, C. Lacefield, W. B. Gruber, R. S. Mann, R. M. Bruno, E. M. Hillman, *Nat. Photonics* **2015**, *9*, 113.
- [22] R. M. Power, J. Huisken, *Nat. Methods* **2017**, *14*, 360.
- [23] A. L. P. S. Carlos Cruz Perez, *J. Biomed. Opt.* **2015**, *20*, 20.
- [24] R. Prevedel, *Nat. Methods* **2014**, *11*, 727.
- [25] Z. Chen, X. L. Deán-Ben, S. Gottschalk, D. Razansky, *Opt. Lett.* **2017**, *42*, 4577.
- [26] X. L. Deán-Ben, T. F. Fehm, S. J. Ford, S. Gottschalk, D. Razansky, *Light: Sci. Appl.* **2017**, *6*, e16247.
- [27] A. Ozbek, X. L. Dean-Ben, D. Razansky, *Optica* **2018**, *5*, 857.
- [28] Z. Chen, X. L. Deán-Ben, S. Gottschalk, D. Razansky, *Biomed. Opt. Express* **2018**, *9*, 2229.
- [29] E. Wang, C. M. Babbey, K. W. Dunn, *J. Microsc.* **2005**, *218*, 148.
- [30] R. Graf, J. Rietdorf, T. Zimmermann, *Adv. Biochem. Eng. Biotechnol.* **2005**, *95*, 57.
- [31] F. Bergermann, L. Alber, S. J. Sahl, J. Engelhardt, S. W. Hell, *Opt. Express* **2015**, *23*, 211.
- [32] J. N. Stirman, I. T. Smith, M. W. Kudenov, S. L. Smith, *Nat. Biotechnol.* **2016**, *34*, 857.
- [33] R. Niesner, V. Andresen, J. Neumann, H. Spiecker, M. Gunzer, *Biophys. J.* **2007**, *93*, 2519.
- [34] L. Song, H. Lu-Walther, R. Förster, A. Jost, M. Kielhorn, J. Zhou, R. Heintzmann, *Meas. Sci. Technol.* **2016**, *27*, 055401.
- [35] P. W. Winter, A. G. York, D. D. Nogare, M. Ingaramo, R. Christensen, A. Chitnis, G. H. Patterson, H. Shroff, *Optica* **2014**, *1*, 181.

- [36] A. G. York, P. Chandris, D. D. Nogare, J. Head, P. Wawrzusin, R. S. Fischer, A. Chitnis, H. Shroff, *Nat. Methods* **2013**, *10*, 1122.
- [37] M. Ingaramo, A. G. York, P. Wawrzusin, O. Milberg, A. Hong, R. Weigert, H. Shroff, G. H. Patterson, *Proc. Natl. Acad. Sci. USA* **2014**, *111*, 5254.
- [38] M. Wang, H. Z. Kimbrell, A. B. Sholl, D. B. Tulman, K. N. Elfer, T. C. Schlichenmeyer, B. R. Lee, M. Lacey, J. Q. Brown, *Cancer Res.* **2015**, *75*, 4032.
- [39] T. Yoshitake, M. G. Giacomelli, L. M. Quintana, H. Vardeh, L. C. Cahill, B. E. Faulkner-Jones, J. L. Connolly, D. Do, J. G. Fujimoto, *Sci. Rep.* **2018**, *8*, 4476.
- [40] V. Kalchenko, D. Israeli, Y. Kuznetsov, A. Harmelin, *Sci. Rep.* **2015**, *4*, 5839.
- [41] G. R. B. E. Römer, P. Bechtold, *Phys. Procedia* **2014**, *56*, 29.
- [42] J. Bewersdorf, R. Pick, S. W. Hell, *Opt. Lett.* **1998**, *23*, 655.
- [43] H. J. Tiziani, R. Achi, R. N. Krämer, T. Hessler, M. T. Gale, M. Rossi, R. E. Kunz, *Opt. Laser Technol.* **1997**, *29*, 85.